Geophysical Journal International

Geophys. J. Int. (2021) **225,** 329–341
Advance Access publication 2020 November 28
GJI Seismology

doi: 10.1093/gji/ggaa567

A new catalogue of toroidal-mode overtone splitting function measurements

Simon Schneider and Arwen Deuss

Department of Earth Sciences, Utrecht University, 3584CB, Princetonlaan 8A, 3582CB Utrecht, The Netherlands. E-mail: s.a.schneider@mailbox.org

Accepted 2020 November 19. Received 2020 November 3; in original form 2020 June 29

SUMMARY

Spectra of whole Earth oscillations or normal modes provide important constraints on Earth's large-scale structure. The most convenient way to include normal mode constraints in global tomographic models is by using splitting functions or structure coefficients, which describe how the frequency of a specific mode varies regionally. Splitting functions constrain 3-D variations in velocity, density structure and boundary topography. They may also constrain anisotropy, especially when combining information from spheroidal modes, which are mainly sensitive to *P–SV* structure, with toroidal modes, mainly sensitive to *SH* structure. Spheroidal modes have been measured extensively, but toroidal modes have proven to be much more difficult and as a result only a limited number of toroidal modes have been measured so far. Here, we expand previous splitting function studies, by focusing specifically on toroidal-mode overtone observations. We present splitting function measurements for 19 self-coupled toroidal modes of which 13 modes have not been measured before. They are derived from radial and transverse horizontal component normal mode spectra up to 5 mHz for 91 events with $M_W \geq 7.4$ from the years 1983–2018. Our data include the Tohoku event of 2011 ($9.1M_W$), the Okhotsk event of 2013 ($8.3M_W$) and the Fiji Island event from 2018 ($8.2M_W$). Our measurements provide new constraints on upper- and lower-mantle shear wave velocity structure and in combination with existing spheroidal mode measurements can be used in future inversions for anisotropic mantle structure. Our new splitting function coefficient data set will be available online.

Key words: Mantle processes; Seismic anisotropy; Seismic tomography; Surface waves and free oscillations.

1 INTRODUCTION

Studying the splitting of whole Earth oscillations enables us to recover large-scale averages of the Earth's *P*- and *S*-wave velocity, density, attenuation and anisotropy. They provide strong constraints on 3-D variations in both isotropic and anisotropic velocity structure of the Earth's mantle and are the only seismic data type directly sensitive to density (Ishii & Tromp 1999; Kuo & Romanowicz 2002; Resovsky & Trampert 2003; Trampert *et al.* 2004; Koelemeijer *et al.* 2017). Normal modes are most easily measured with the splitting function approach (i.e. Woodhouse & Giardini 1985) using least-squares inversion of normal mode spectra. Splitting function coefficients are linearly dependent on 3-D variations of Earth's structure, and are easily included in tomographic inversion for mantle velocity structure (e.g. Ritsema *et al.* 2011; Moulik & Ekström 2014; Koelemeijer *et al.* 2015).

So far splitting functions have mainly been measured for spheroidal modes which are mainly sensitive to *P*-wave and vertically polarized *S*-wave velocity (*P–SV*) and are able to constrain velocity and density structure in the mantle and core (e.g. Giardini *et al.* 1988; Roult *et al.* 1990; He & Tromp 1996; Resovsky & Ritzwoller 1998; Durek & Romanowicz 1999; Deuss *et al.* 2010, 2013; Koelemeijer *et al.* 2013). Spheroidal modes are clearly visible in normal mode spectra of vertical component seismograms, which have relatively low noise levels making it easy to measure them. Splitting functions of more than 180 spheroidal modes in the frequency range up to 10 mHz have been measured thus far.

Splitting functions for toroidal modes have not been measured very much and only a few toroidal-mode splitting function measurements exist (Derr 1969; Widmer *et al.* 1992; Masters & Widmer 1995; Tromp & Zanzerkia 1995; Resovsky & Ritzwoller 1998). The problem with toroidal modes is that we need horizontal component seismograms, which contain much more noise, for example, due to atmospherically induced tilting, making it much more difficult to make measurements. Splitting functions for around 30 toroidal modes in the frequency range up to 3 mHz have been measured so far, which is much less than the spheroidal modes. The importance of toroidal modes is that they are mainly sensitive to

horizontally polarized *S*-wave (*SH*) velocity, which in combination with spheroidal modes (sensitive to *P–SV*) constrains radial and azimuthal anisotropy (e.g. Beghein *et al.* 2008).

Seismic anisotropy means that the velocity of a seismic wave depends on the travelling or polarization direction. The importance of anisotropy is that it gives us a way to interpret seismic directional information of Earth's interior in terms of mantle flow (e.g. Long & Becker 2010). It is well known from surface wave studies that radial anisotropy exists in the crust, lithosphere and upper mantle (Montagner & Tanimoto 1991; Ekström & Dziewonski 1998; Vinnik *et al.* 1998; Lebedev *et al.* 2009; Russell *et al.* 2019). More recent global models, also incorporating body waves, suggest the existence of radial anisotropy in the transition zone and core–mantle boundary D″ region (Panning & Romanowicz 2006; Chang *et al.* 2014; French & Romanowicz 2014; Moulik & Ekström 2014). Azimuthal anisotropy is less often studied, but it has been observed in the lithosphere (Smith & Dahlen 1973; Tanimoto & Anderson 1985; Marone & Romanowicz 2007; Schaeffer *et al.* 2016) and sometimes even in the transition zone (Trampert & van Heijst 2002; Yuan & Beghein 2014). Even though most models agree on the existence of radial and azimuthal anisotropy in the lithosphere, much less consensus exists about the need for anisotropy in the transition zone and core–mantle boundary region.

In order to constrain anisotropy in these deeper parts of the mantle, normal-mode overtones are essential because they are sensitive to the whole mantle, as well as density and boundary topography. Only very few studies have incorporated normal modes in making anisotropy models. Beghein *et al.* (2008) used the observed cross-coupled splitting between fundamental spheroidal and toroidal modes to determine whether the data are compatible with azimuthal anisotropy below 400 km. Moulik & Ekström (2014) used spheroidal- and toroidal-modes splitting function observations as well as surface waves and body waves to construct a velocity model of the Earth's mantle; they found strong radial anisotropy in the uppermost 300 km of the mantle and some evidence for regionally varying radial anisotropy in the transition zone and lowermost mantle.

Unfortunately, these studies were only able to use a small number of relatively old toroidal-mode measurements, because toroidal modes have not been measured for more than 20 yr, since the studies of Widmer *et al.* (1992), Tromp & Zanzerkia (1995) and Resovsky & Ritzwoller (1998). In order to robustly constrain radial and azimuthal anisotropy in the transition zone and lower mantle, we need more toroidal-mode measurements. Recent studies of toroidal modes have been conducted using ring-laser instruments by Igel *et al.* (2011) investigating the 2011 Tohoku earthquake, but mainly focused on the newly available technology.

In the last 20 yr, the global seismic network was significantly increased and a number of large earthquakes have happened (see Table 1). Therefore, now it is a good time to remeasure the toroidal modes and also investigate if new toroidal modes can be observed that have not been measured before. Here, we will expand the more recent study by Deuss *et al.* (2013), that only used vertical components to measure spheroidal modes, by collecting horizontal component data for all large earthquakes from the last 35 yr (see Fig. 1 and Table 1). We are using our new horizontal data recordings to refine and extend self-coupling splitting function measurements of isolated toroidal overtones which are only visible on the horizontal component of the seismogram.

It is well known that modes are strongly cross-coupled to nearby modes (e.g. Deuss & Woodhouse 2001). However, measuring toroidal-mode splitting functions using horizontal component data

Table 1. List of events used in this study. Date is day/month/year, depth is in km, M_W is the moment magnitude from the CMT catalogue and N_R and N_T denote the numbers of stations for the radial and transversal component per event.

Date	Location	Depth	M_W	N_T	N_R
19/08/2018	Fiji Islands	555.00	8.2	9	5
08/09/2017	Chiapas Mexico	50.20	8.2	3	3
25/12/2016	Southern Chile	32.80	7.6	2	1
29/07/2016	Mariana Islands	208.90	7.7	8	5
26/10/2015	Hindu Kush Afghanistan	209.40	7.5	1	1
16/09/2015	Central Chile	17.40	8.3	14	8
30/05/2015	Bonin Islands	680.70	7.9	21	14
05/05/2015	New Britain	38.30	7.5	5	2
17/11/2013	Scotia Sea	23.80	7.8	6	6
24/05/2013	Sea Of Okhotsk	611.00	8.3	74	64
05/09/2012	Costa Rica	29.70	7.6	11	7
31/08/2012	Philippines	45.20	7.6	12	3
27/08/2012	Central America	12.00	7.3	10	6
14/08/2012	Sea Of Okhotsk	598.20	7.7	11	7
11/03/2011	Honshu Japan	20.00	9.1	73	14
27/02/2010	Central Chile	23.20	8.8	22	77
05/07/2008	Sea Of Okhotsk	610.80	7.7	42	46
12/05/2008	Sichuan China	12.80	7.9	69	61
09/12/2007	South Of Fiji Islands	149.90	7.8	46	42
14/11/2007	Northern Chile	37.60	7.7	34	28
28/09/2007	Volcano Islands	275.80	7.5	30	26
15/08/2007	Coast Of Peru	33.80	8.0	59	53
08/08/2007	Java Indonesia	304.80	7.5	26	34
01/04/2007	Solomon Islands	14.10	8.1	70	59
13/01/2007	East Kuril	12.00	8.1	68	57
15/11/2006	Kuril Islands	13.50	8.3	85	70
17/07/2006	South Of Java	20.00	7.7	35	32
03/05/2006	Tonga Islands	67.80	8.0	52	38
20/04/2006	Eastern Siberia	12.00	7.6	47	33
27/01/2006	Banda Sea	397.40	7.6	36	33
08/10/2005	Pakistan	12.00	7.6	43	40
26/09/2005	Northern Peru	108.10	7.5	34	37
09/09/2005	New Ireland	83.60	7.6	34	25
28/03/2005	Northern Sumatra	25.80	8.6	94	73
23/12/2004	North Macquarie	27.50	8.1	24	0
17/11/2003	Rat Islands	21.70	7.7	32	28
25/09/2003	Hokkaido Japan	28.20	8.3	12	10
04/08/2003	Scotia Sea	15.00	7.6	38	33
15/07/2003	Carlsberg Ridge	15.00	7.5	40	33
03/11/2002	Central Alaska	15.00	7.8	58	43
08/09/2002	Papua New Guinea	19.50	7.6	39	24
19/08/2002	South Of Fiji	699.30	7.7	48	44
14/11/2001	Qinghai China	15.00	7.8	49	40
07/07/2001	Coast Of Peru	25.00	7.6	29	25
23/06/2001	Coast Of Peru	29.60	8.4	66	59
26/01/2001	India	19.80	7.6	41	26
13/01/2001	El Salvador	56.00	7.7	42	32
18/06/2000	South Indian Ocean	15.00	7.9	61	44
04/06/2000	Southern Sumatra	43.90	7.8	51	37
28/03/2000	Volcano Islands	99.70	7.6	35	29
20/09/1999	Taiwan	21.20	7.6	22	19
17/08/1999	Turkey	17.00	7.6	32	25
29/11/1998	Ceram Sea	16.40	7.7	29	36
25/03/1998	Balleny Islands	28.80	8.1	60	62
04/01/1998	Loyalty Islands	114.30	7.4	22	13
05/12/1997	Kamchatka	33.60	7.8	49	30
08/11/1997	Tibet	16.40	7.5	21	21
14/10/1997	South Of Fiji Islands	165.90	7.7	19	14
12/11/1996	Coast Of Peru	37.40	7.7	36	24
17/06/1996	Flores Sea	584.20	7.8	43	38
10/06/1996	Andreanof Islands	29.00	7.9	9	11
17/02/1996	West Irian	15.00	8.2	37	22

Table 1. Continued

Date	Location	Depth	M_W	N_T	N_R
01/01/1996	Minahassa Peninsula	15.00	7.9	23	19
03/12/1995	Kuril Islands	25.90	7.9	36	30
09/10/1995	Jalisco Mexico	15.00	8.0	34	24
30/07/1995	Northern Chile	28.70	8.0	46	38
28/12/1994	Coast Of Honshu	27.70	7.7	18	20
04/10/1994	Kuril Islands	68.20	8.3	45	42
09/06/1994	Northern Bolivia	647.10	8.2	52	41
02/06/1994	South Of Java	15.00	7.8	14	9
09/03/1994	Fiji Islands	567.80	7.6	24	14
12/07/1993	Hokkaido Japan	16.50	7.7	27	23
15/01/1993	Hokkaido Japan	100.00	7.6	14	12
12/12/1992	Flores Island	20.40	7.7	18	18
11/10/1992	Vanuatu	141.10	7.4	12	3
02/09/1992	Nicaragua	15.00	7.6	17	11
22/12/1991	Kuril Islands	31.20	7.6	8	4
22/04/1991	Costa Rica	15.00	7.6	5	5
30/12/1990	New Britain	204.80	7.4	2	1
16/07/1990	Luzon Philippines	15.00	7.7	7	4
18/04/1990	Minahassa Peninsula	33.20	7.6	2	2
03/03/1990	South Of Fiji Islands	25.30	7.6	3	1
23/05/1989	Macquarie Islands	15.00	8.0	3	0
06/03/1988	Gulf Of Alaska	15.00	7.7	4	1
30/11/1987	Gulf Of Alaska	15.00	7.8	2	0
20/10/1986	Kermadec Islands	50.40	7.7	4	0
07/05/1986	Andreanof Islands	31.30	7.9	2	1
03/03/1985	Central Chile	40.70	7.9	1	0
06/03/1984	Honshu Japan	446.00	7.4	1	0
24/11/1983	Banda Sea	157.10	7.4	1	1

is challenging, so in this paper we only selected modes that can be treated as self-coupled to simplify the measurement process. Measuring larger groups of modes in cross-coupling, or even wide-band coupling, is computational expensive as the splitting matrix grows with each additional mode. Splitting functions can only do so much and measurements of self-coupled modes are a good starting point for future inversions. We carefully selected toroidal-mode overtones that are sufficiently separated in frequency from neighbouring modes. We included cross-coupling due to rotation and ellipticity of the Earth to neighbouring modes in some cases (see Table 2) and ensured that all these modes showed none or negligible structural cross-coupling to the overtone measured in self-coupling. For this reason we only measured toroidal overtones, because the fundamental toroidal modes are strongly cross-coupled to fundamental spheroidal modes. These need to be measured in cross-coupled pairs by combining both vertical and horizontal component data, which will be the subject of a separate paper.

2 THEORY AND METHOD

After a strong earthquake occurs, the whole Earth reverberates or rings like a bell. The resulting whole Earth oscillations are standing waves along Earth's surface and radius. They are called normal modes and only exist for discrete frequencies, where individual modes are identified by their angular order l and radial order or overtone number n, with $n = 0$ for fundamental modes and $n \geq 1$ for the overtone branches. Constant n values span overtone branches (Fig. 2). Normal modes can be divided into two types: (i) spheroidal modes ${}_nS_l$, involving vertical and horizontal surface motion, comparable to *P–SV* wave motion or Rayleigh waves and (ii) toroidal modes ${}_nT_l$, involving only horizontal surface motion, comparable to *SH* wave motion or Love waves. Here, we will focus on isolated toroidal overtones ${}_{n\geq 1}T_l$; the measurement of the fundamentals will be the subject of a separate paper.

Each mode of overtone number n and angular order l consists of $2l + 1$ singlets. The singlets are labelled by the azimuthal order m, with $-l \leq m \leq l$. In a spherical, non-rotating, elastic and isotropic (SNREI) Earth, such as the Preliminary Reference Earth Model (PREM, Dziewonski & Anderson 1981), all singlet frequencies of a mode are identical. This is called degeneracy. Deviations from the SNREI Earth change the singlet frequencies of the mode, so they all get different values. This is called splitting and is caused by rotation of the Earth, ellipticity and 3-D variations in velocity, density, anisotropy and attenuation. Splitting of isolated modes is called self-coupling; splitting caused by the resonance of two or more modes is called cross-coupling. Here, we focus on the self-coupling approximation and only measure toroidal modes that are separated enough from other modes in frequency so that cross-coupling can be ignored and they can be measured as isolated.

The splitting of normal modes is fully described using the splitting function approach, which was introduced by Woodhouse & Giardini (1985) and extended to the generalized splitting function approach including cross-coupling by Resovsky & Ritzwoller (1998). Masters *et al.* (2000a) introduced a source independent method, called autoregressive estimation, which was recently used to measure spheroidal mode splitting functions including uncertainties (Pachhai *et al.* 2015). This method requires the number of events to be proportional to the angular order l of the measured mode. This is unfeasible for modes with a higher l. Therefore we use the conventional method also used in Woodhouse & Giardini (1985), He & Tromp (1996), Resovsky & Ritzwoller (1998) and Deuss *et al.* (2013).

Splitting functions are defined by elastic coefficients c_{st}, which are linearly dependent on 3-D variations in compressional velocity v_p, shear wave velocity v_s and density with respect to the reference Earth model, that is, PREM. In principle it should also be possible to measure anelastic splitting function coefficients d_{st} (i.e. Masters *et al.* 2000b; Mäkinen & Deuss 2013), which are linearly dependent on 3-D variations in shear attenuation q_μ and bulk attenuation q_κ. However, we ignore anelastic splitting function observations for now, because current horizontal components data are still too noisy to make measurement possible. The relation relating the elastic splitting function coefficients c_{st} to 3-D variations in mantle structure can be expressed using:

$$c_{st} = \int_0^a \delta m_{st}(r) K_s(r) dr + \sum_d \delta h^d_{st} H^d_s \tag{1}$$

where δm_{st} are the spherical harmonic coefficients of angular order s and azimuthal order t of the Earth's heterogeneity (v_p, v_s and ρ) and δh^d_{st} the coefficients of discontinuity topography. $K_s(r)$ and H^d_s are known sensitivity kernels (Woodhouse 1980). To visualize splitting functions, we use splitting function maps $F(\theta, \Phi)$, defined as

$$F(\theta, \Phi) = \sum_{s=0}^{2l} \sum_{t=-s}^{s} c_{st} Y^t_s(\theta, \Phi) \tag{2}$$

where $Y^t_s(\theta, \Phi)$ are the complex spherical harmonics (Edmonds 1960).

We measure the splitting function coefficients from large numbers of observed horizontal component spectra of large earthquakes. The spectra depend nonlinearly on the splitting function coefficients, and therefore we employ a nonlinear iterative least-squares inversion (Tarantola & Valette 1982). For details of our method see Deuss *et al.* (2013). Because of the nonlinearity of the inversion we started

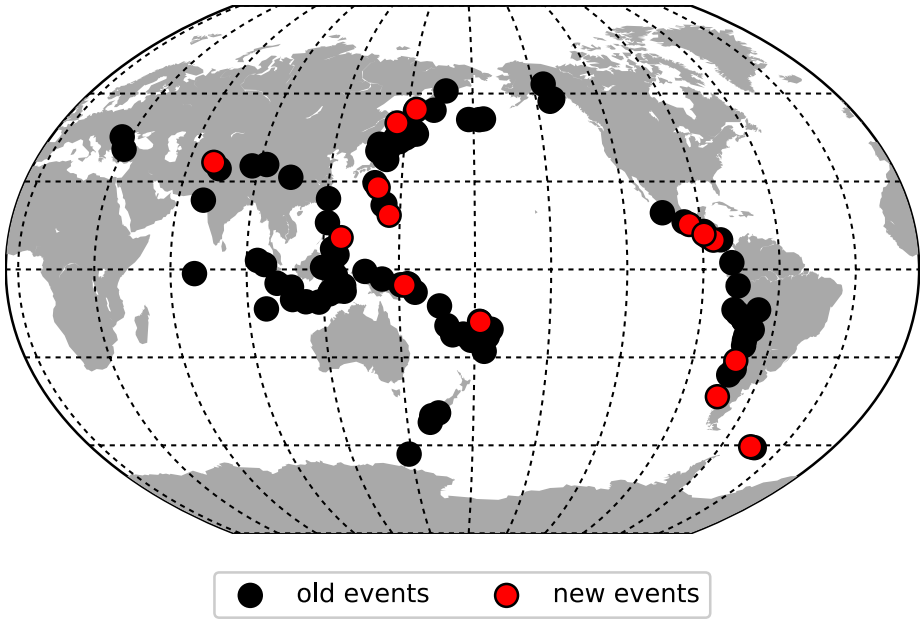

Figure 1. Locations of the 91 events used in this study. Red circles mark new events which were not included in previous splitting function studies.

Table 2. Misfit for normal-mode spectra used in this study. Modes between brackets were included in the measurement procedure for completeness, but their splitting functions are not constrained well enough by the data to be reported. $s_{\max}$ denotes the highest specified spherical harmonic degree, $N_{\rm ev}$ denotes the number of events, N_T the number of transverse component spectral records and N_R the number radial component records. PREM denotes the misfit including only rotation and ellipticity of the Earth, seperated in transverse (m^T) and radial component (m^R) misfit. The misfits for the S20RTS model and after c_{st} measurement are also given.

Spectral segment	$s_{\max}$	$N_{\rm ev}$	N_T	N_R	PREM		S20RTS		c_{st}	
					m^T	m^R	m^T	m^R	m^T	m^R
${}_1T_2$	4	14	84	41	0.50	0.52	0.32	0.33	0.27	0.28
${}_1T_3$	6	20	94	59	0.45	0.56	0.39	0.42	0.34	0.35
${}_1T_5$-(${}_0S_{10}$, ${}_0T_{11}$)	4	66	428	233	0.59	0.74	0.55	0.70	0.52	0.66
${}_1T_6$	6	52	221	144	0.84	0.83	0.57	0.69	0.46	0.55
${}_1T_7$-(${}_0S_{13}$, ${}_0T_{14}$, ${}_5S_2$)	10	77	847	1241	0.76	0.63	0.71	0.62	0.68	0.60
${}_1T_{13}$-(${}_0S_{22}$, ${}_0T_{23}$, ${}_6S_4$)	6	70	497	472	0.72	0.78	0.63	0.73	0.58	0.70
${}_1T_{14}$-(${}_0S_{24}$, ${}_0T_{25}$, ${}_2S_{15}$)	6	77	690	1192	0.84	0.65	0.76	0.63	0.72	0.62
${}_2T_3$-(${}_1T_8$, ${}_4S_4$)	2	19	34	34	0.71	0.76	0.73	0.73	0.57	0.62
${}_2T_5$	2	45	99	43	0.84	0.91	0.73	0.89	0.62	0.85
${}_2T_7$	6	42	129	60	1.05	0.99	0.83	0.91	0.74	0.88
${}_2T_8$-(${}_0S_{20}$, ${}_0T_{21}$, ${}_2S_{13}$)	6	56	226	224	1.05	0.87	0.77	0.77	0.68	0.72
${}_2T_{13}$-(${}_0T_{29}$, ${}_0S_{30}$)	4	57	152	274	0.99	0.73	0.82	0.69	0.79	0.68
${}_2T_{14}$-(${}_4S_{11}$, ${}_1T_{19}$)	4	62	220	230	0.86	0.74	0.70	0.72	0.62	0.67
${}_2T_{15}$	4	50	96	109	1.01	0.96	0.77	0.91	0.71	0.83
${}_2T_{16}$-(${}_4T_3$, ${}_1S_{23}$, ${}_{10}S_4$)	2	42	77	52	1.03	0.96	0.84	0.93	0.79	0.89
${}_3T_1$-(${}_9S_1$, ${}_8S_2$, ${}_0T_{24}$, ${}_0S_{23}$)	2	28	72	65	0.48	0.66	0.49	0.61	0.48	0.59
${}_3T_7$	2	48	96	110	0.96	1.00	0.87	0.91	0.80	0.86
${}_3T_{16}$-(${}_2T_{20}$, ${}_4S_{18}$)	2	17	20	24	0.85	0.86	0.69	0.83	0.66	0.81
${}_4T_9$-(${}_3S_{21}$, ${}_7S_{10}$, ${}_{11}S_4$)	2	11	12	189	0.71	0.57	0.72	0.56	0.68	0.54

all our splitting function measurements from two different different starting models and apply a range of norm damping parameters encompassing several order of magnitude. Our two starting models are (i) PREM, so all splitting function coefficient c_{st} starting values are zero and (ii) using non-zero c_{st} splitting function coefficients calculated for tomographic mantle model S20RTS + CRUST5.1 (called S20RTS from here on, Ritsema *et al.* 2011). In all starting models rotation and ellipticity were also included. We selected our results depending which of the two starting models resulted in the lowest misfit, and in case both had the same misfit reduction, the PREM starting model was selected. We iterate each run 10–20 times and investigate the trade-off between model size and misfit as a function of damping and pick the best compromise. In most cases, the inversion did not require starting from S20RTS mantle predictions, and we were able to measure splitting function coefficients starting from PREM with only ellipticity and rotation. For completeness we include nearby modes for ellipticity and rotational coupling (see Table 2), but do not invert for splitting function coefficients of these additional modes. We edited all seismic data by hand for bias control and to ensure sufficient data quality, which includes removal of delta spikes in the time-series. We assigned uncertainties for all our measurements using the cross-validation method as described

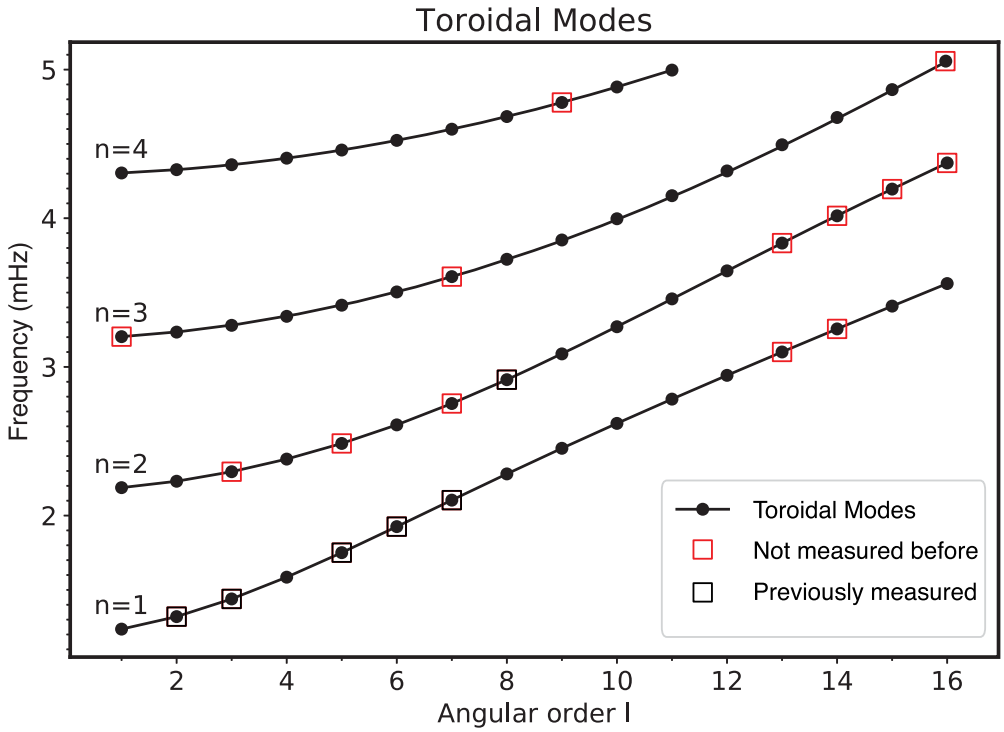

Figure 2. Frequency versus angular order l of the measured modes. Red squares indicate toroidal-mode overtones measured here, black squares denote modes measured here, for which splitting functions have been measured before by Tromp & Zanzerkia (1995) and Resovsky & Ritzwoller (1998).

in Deuss *et al.* (2013), where we leave out whole events in different cross-validation runs. This method removes whole earthquakes at a time, we checked therefore for influence of individual earthquake sources on our measurements. To reduce theoretical errors from unspecified higher degree structures, we measured all modes to the highest degree possible, often higher than we report. To evaluate our measurements, we define the misfit between the data d_i and the synthetics u_i including our new splitting function coefficients, as

$$\text{misfit} = \frac{1}{N}\sum^{N}\frac{\sum_{i=1}^{n}(d_i - u_i(c_{st}))^2}{\sum_{i=1}^{n} d_i^2} \tag{3}$$

with N spectral segments for each mode and n data points per segment.

3 DATA

Due to the long period of normal modes, we require several day-long, good quality waveform data to make toroidal-mode observations and measure splitting functions. Normal modes are observed in the frequency domain, so we Fourier transform the time-domain waveform data to the frequency domain. Normal modes are most clearly observed after large earthquakes (Fig. 1 and Table 1), 14 of which are newly added to the existing data set of Deuss *et al.* (2013). We dismissed data of events before 1983 because horizontal component data were either not available or from very poor quality. Our new events include the 2013 Okhotsk earthquake ($M_W = 8.3$) and the continental 2015 Hindu Kush, Afghanistan ($M_W = 7.5$) earthquake. For our final amount of data for each earthquake, see Table 1.

Toroidal modes are most clearly observed on the horizontal component of the seismic data. We rotated the horizontal north and east components to their theoretical backazimuth in order to obtain radial (R) and transverse (T) components and isolate toroidal-mode signals. In theory, we expect the horizontal motion of toroidal modes due to their *SH* wave nature to show up most clearly on the transverse component and for example, Tromp & Zanzerkia (1995) only used transverse component data in their toroidal-mode measurements. We expect to see a mix of toroidal- and spheroidal-mode signals on the radial component due to the *P–SV*-wave like nature of spheroidal modes. We will use both transverse and radial components in our inversion.

All modes measured here show up as isolated spectral peaks and are well separated from spheroidal modes in the frequency spectrum from 1 to 5 mHz. Selecting horizontal component data is more complicated than vertical component data. The data quality is often poorer compared to vertical component data because of more noise due to atmospherically induced tilting. The peaks appear less sharp, often with lower amplitude and the spectrum has in general a lower signal-to-noise ratio (SNR). One example is given in Fig. 3, showing the amplitude spectra of the $M_W = 9.1$ Tohoku, Japan event of 2011, observed in Canberra, Australia. The amplitude of the signal between the dominant peaks is lower for the vertical (VHZ) component than for the horizontal components (VHR and VHT). The difference becomes even more dramatic for higher frequencies, and for smaller events noise also starts overwhelming the toroidal-mode peaks on the horizontal components. Many modes start overlapping in frequency, which makes it harder to make clear observations of our toroidal-mode overtones and corresponding splitting function measurements.

The large noise signal on horizontal component data may be due to barometric pressure (Steffen *et al.* 2006). The noise level can be reduced in future applications when new instruments may become available (Ringler *et al.* 2015), or using linear strain meters (Zürn *et al.* 2015) or if the setup of the seismometer location is suitable the

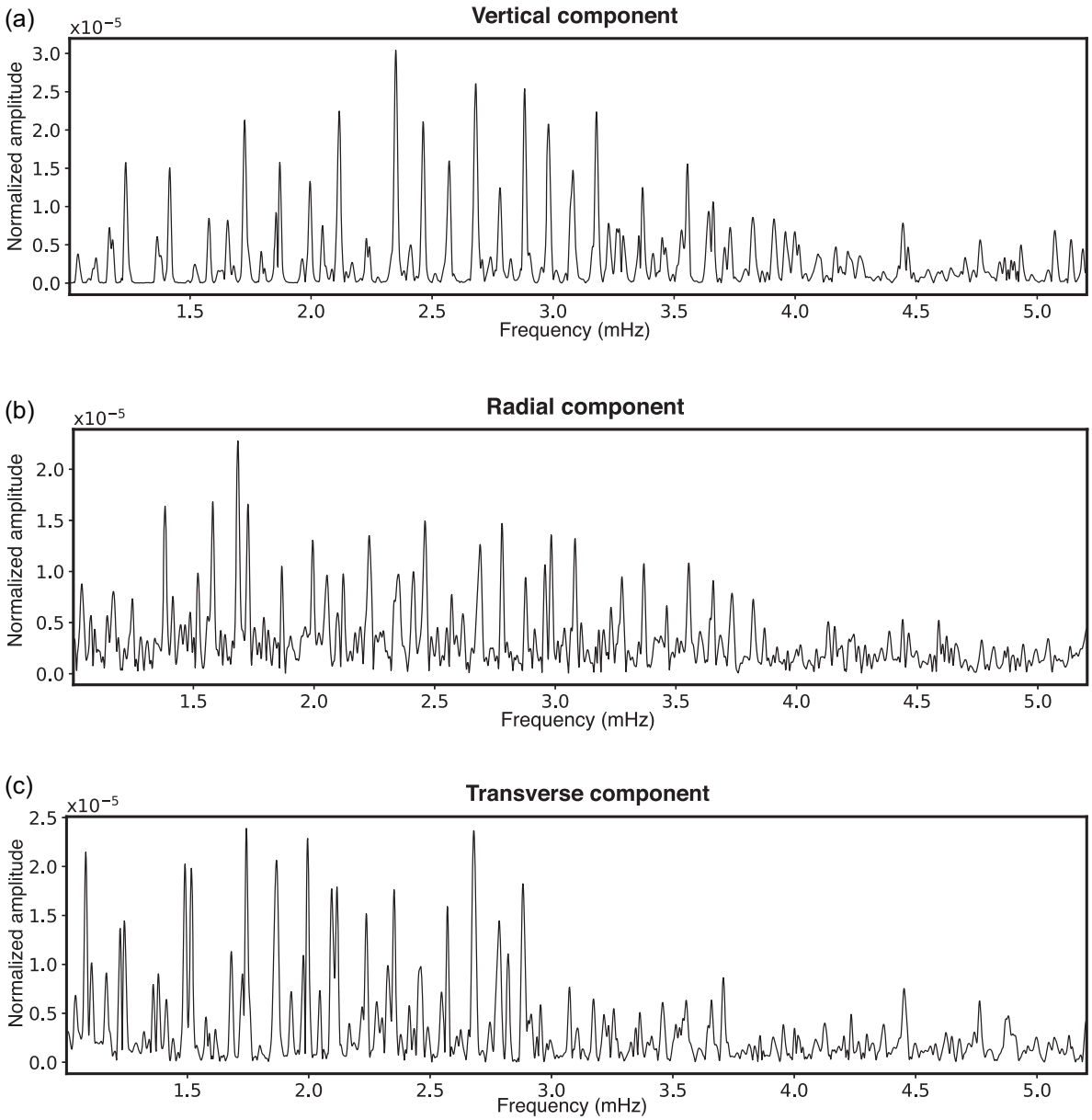

Figure 3. Observed spectra for time series of 5–45 hr length, for the large magnitude $M_W = 9.1$ Tohoku event of 2011, showing (a) the vertical, (b) radial and (c) transverse components.

SNR can be improved by common array stacking methods (Ringler *et al.* 2016). We could not yet take advantage of new instruments or stacking methods, hence we must take advantage of all currently available data on IRIS. It is important to note that due to the low SNR of the horizontal component data, we cautiously selected our records by hand in an extensive process. An example of our selected spectral segments is shown in Fig. 4 for mode ${}_1T_6$. This is an exceptionally clear mode, which is easily observed on both the radial and the transverse components.

4 RESULTS

We measure splitting functions for toroidal overtones in our aim to improve constraints on mantle structure, especially for shear velocity v_s and radial and azimuthal anisotropies. We managed to make splitting functions measurements for toroidal overtones that had not been measured before and improved splitting function measurements for previously measured modes by adding new data. Our measurements include splitting functions for 19 self-coupled toroidal modes, mainly for the first and second overtones and a few third and fourth overtones (see Fig. 2). For six of these modes splitting functions were measured before by Tromp & Zanzerkia (1995, TZ from here on) and/or Resovsky & Ritzwoller (1998, RR from here on). For 12 of these modes centre frequencies and attenuation were measured before by Widmer *et al.* (1992) and Masters & Widmer (1995). We also present 13 new splitting functions which were never measured before.

All our measured toroidal overtones are listed in Table 2 which shows the number of records used in the inversion for each mode, separated into transverse and radial components, the data misfit using PREM with only rotation and ellipticity, the misfit using mantle model S20RTS and crustal model CRUST5.1 and finally the misfit including our newly measured splitting function coefficients.

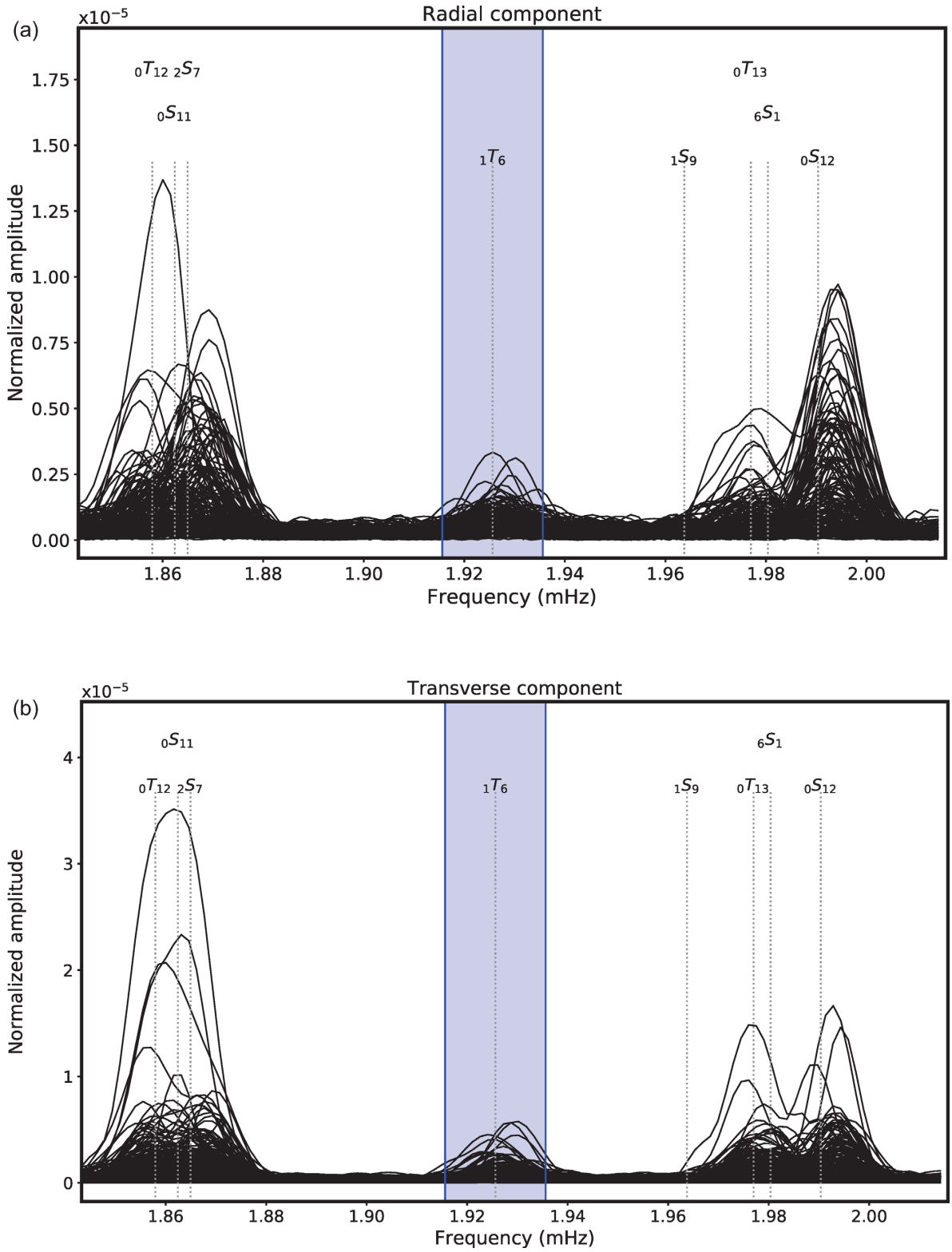

Figure 4. All used spectra (time-series of each has 3–60 hr length), showing (a) the radial and (b) the transverse components for mode $_1T_6$. Highlighted in blue is the used frequency window.

For all measured modes, the c_{st} misfit after our inversion is lower than the PREM misfit including only rotation and ellipticity and also lower than the mantle and crustal model misfit. Two examples for modes $_1T_2$ and $_1T_6$ are shown in Fig. 5 illustrating the improvement of misfit between data and synthetics, comparing synthetic spectra calculated for PREM including only rotation and ellipticity with synthetics including our measured splitting functions coefficients. The amplitude and phase of the splitting function spectra much

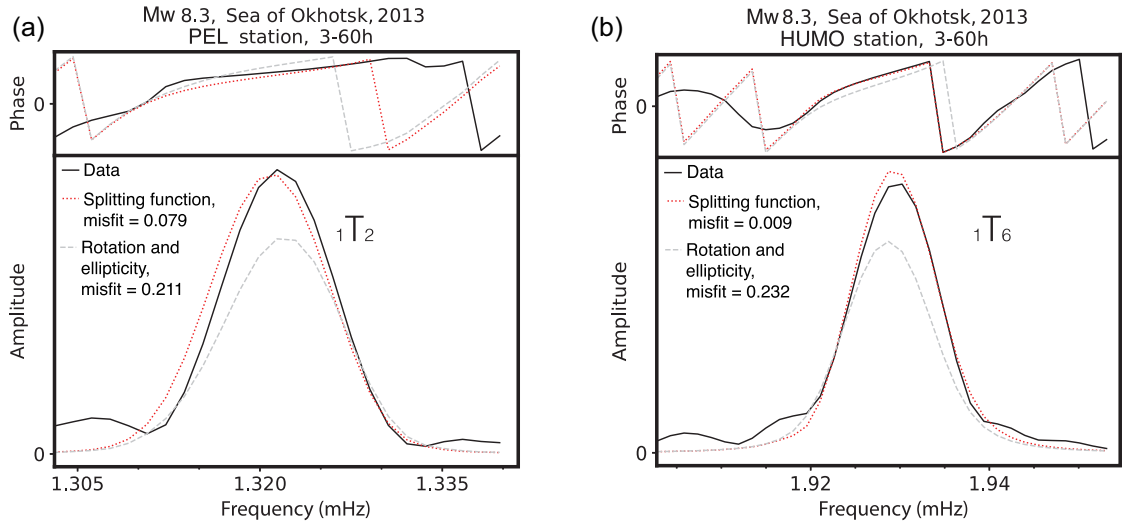

Figure 5. Example of a spectral window, showing observed data, PREM model prediction including rotation and ellipticity, and synthetics calculated using our measured splitting function (also including rotation and ellipticity) for (a) $_1T_2$ and (b) $_1T_6$.

Table 3. Centre frequencies in μHz and quality factors Q for the toroidal modes measured in this study. Also shown are PREM values (f_0, Q_0)

Mode	PREM f_0 (μHz)	Measured f_c (μHz)	PREM Q_0	Measured Q
$_1T_2$	1320.13	1319.29 ± 0.17	256	302 ± 19
$_1T_3$	1439.13	1438.45 ± 0.08	253	299 ± 7
$_1T_5$	1750.49	1750.19 ± 0.13	246	303 ± 9
$_1T_6$	1925.61	1925.25 ± 0.12	242	277 ± 7
$_1T_7$	2103.79	2103.40 ± 0.06	237	289 ± 3
$_1T_{13}$	3100.46	3099.07 ± 0.10	215	236 ± 3
$_1T_{14}$	3255.59	3253.52 ± 0.06	213	227 ± 2
$_2T_3$	2294.97	2295.28 ± 0.22	207	236 ± 7
$_2T_5$	2485.09	2484.87 ± 0.15	213	245 ± 5
$_2T_7$	2753.73	2753.00 ± 0.33	223	247 ± 12
$_2T_8$	2913.97	2912.57 ± 0.08	229	267 ± 3
$_2T_{13}$	3832.88	3830.52 ± 0.21	242	271 ± 7
$_2T_{14}$	4016.39	4013.81 ± 0.24	241	301 ± 8
$_2T_{15}$	4196.12	4192.69 ± 0.22	239	287 ± 7
$_2T_{16}$	4372.15	4368.75 ± 0.53	237	258 ± 15
$_3T_1$	3203.50	3200.08 ± 1.73	216	203 ± 52
$_3T_7$	3607.30	3603.68 ± 0.24	228	286 ± 8
$_3T_{16}$	5054.35	5051.39 ± 0.23	243	273 ± 6
$_4T_9$	4778.82	4775.37 ± 1.86	221	237 ± 38

better match the observed spectra than the PREM spectra and the misfit is also significantly lower.

4.1 Centre frequency and Q values

The centre frequencies and Q values of all our measured toroidal overtones are shown in Table 3 and Fig. 6. Centre frequency and Q values provide information about the 1-D velocity, density and attenuation structure of the Earth. Our centre frequency values (Fig. 6a) are often similar to previous measurements; when they differ, our new measurements are often more branch consistent. For almost all our measured toroidal overtones (except $_2T_3$), we observe centre frequencies that are lower than PREM. Comparing our centre frequencies to previous measurements and model predictions, we find that our observations are right in between the previous measurements of Tromp & Zanzerkia (1995) and Resovsky & Ritzwoller (1998). For the first overtone and part of the second overtone, we observe higher centre frequencies than predicted by S20RTS and also almost always higher than observed by RR. On the other hand, we often observe lower frequencies than those observed by TZ. From $_2T_8$ onward, we observe higher centre frequencies which are more similar to PREM than those observed by Masters & Widmer (1995), and lower centre frequencies than predicted by S20RTS, except for $_3T_1$ and $_4T_9$, but these modes also have the largest errors. As we are using the same method, we attribute these differences most likely to the larger size of the data set used in our study, which counts for all measured modes at least twice the amount of spectra compared to Tromp & Zanzerkia (1995) and Resovsky & Ritzwoller (1998).

Our Q-value measurements (Fig. 6b) show more scatter than our centre frequency measurements. This is a well-known feature of normal mode measurements due to the fact that the Q values depend on the spectral amplitude which is strongly influenced by noise. Our Q values for the first overtone are always higher than previous measurements by TZ and RR. Only for mode $_2T_8$ our measured Q value is lower then observed by RR, but again note that this mode has large error bars. Also, this mode is complicated by modes $_0S_{20}$, $_0T_{21}$ and $_2S_{13}$ which are nearby in frequency. Measurements of $_2T_8$ might improve when taking cross-coupling with the additional fundamental modes into account.

4.2 Splitting function coefficients

The centre frequency and Q values (i.e. degree $s = 0$ structure) have been measured jointly with splitting function coefficients for larger degrees $s \geq 2$. We measure self-coupled splitting functions, which only exist for even degrees. Splitting function coefficients for $s \geq 2$ provide information on 3-D variations in shear wave velocity and density. In agreement with our centre frequency values, the measured splitting function coefficients for $s = 2$ also show nice branch consistency (Fig. 7).

For completeness we also included modes $_3T_1$ and $_4T_9$ in this paper, which have proven to be difficult to measure due to poor data quality and have to be interpreted with care. This is reflected in their considerably larger error bars and our measurements for these modes are mainly published for comparison with future measurements.

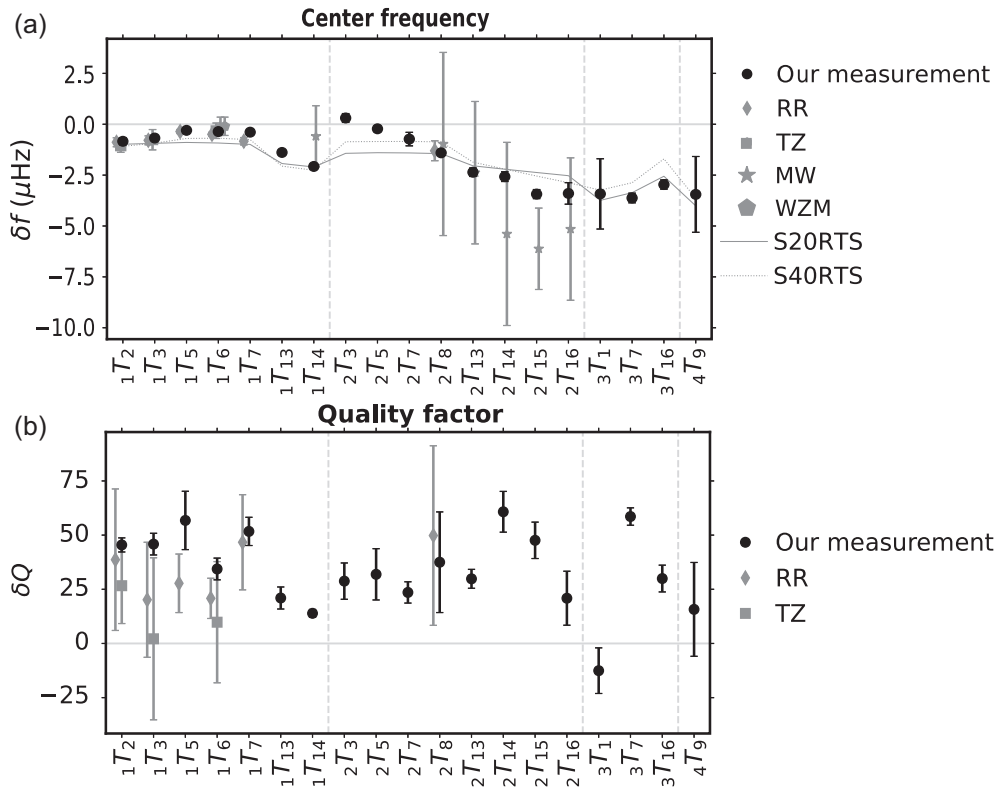

Figure 6. (a) Measured centre frequencies and (b) quality factors with respect to reference model PREM as a function of angular order l for increasing mode branch n. Black circles denote our measurements, also shown are measurements from Resovsky & Ritzwoller (1998, diamonds), Tromp & Zanzerkia (1995, squares), Masters & Widmer (1995, stars) and Widmer *et al.* (1992, pentagons). Model predictions of S20RTS (solid grey line) as well as S40RTS (dashed grey line) are also shown.

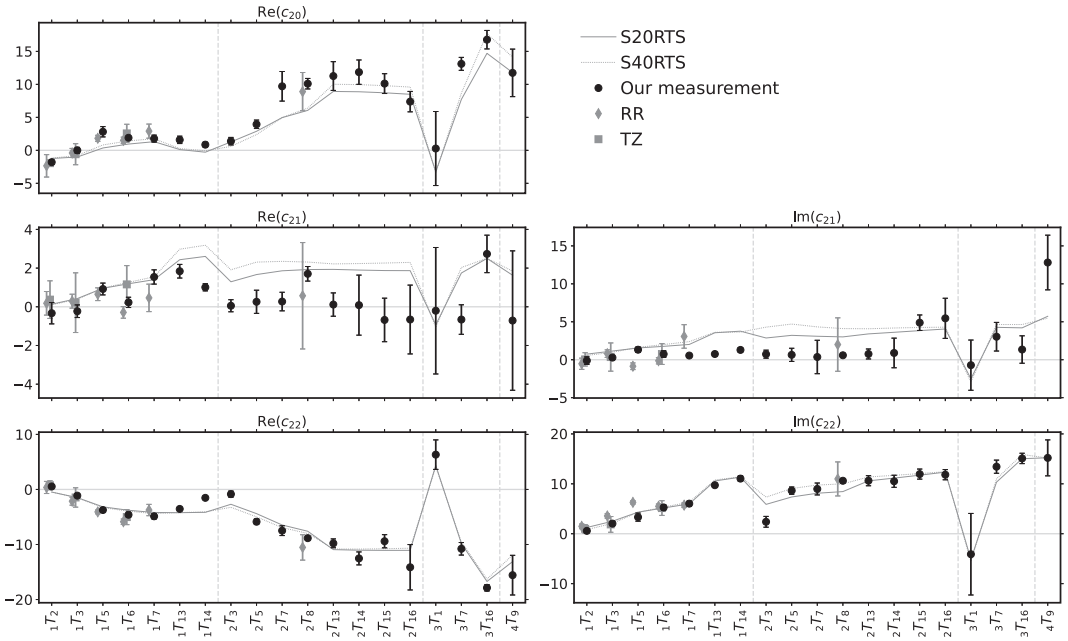

Figure 7. Same as Fig. 6, but for all degree $s = 2$ splitting function coefficients. Vertical dashed lines separate different overtone branches.

The sensitivity kernels of each branch change only smoothly as a function of angular order l (see left-hand columns in Figs 8–10), so we also expect the splitting function coefficients to vary smoothly too along each branch. We find overall consistent branches, especially the largest degree 2 values (c_{20}), Re(c_{22}) and Im(c_{22}), which define the well-known 'ring around the Pacific' structure, show consistency along the branches of each overtone. Comparing our measurements with the S20RTS predictions, we find for example that for the first and second overtone branches, our measurements have larger c_{20} values and smaller Rec_{21} and Imc_{21} values than the model

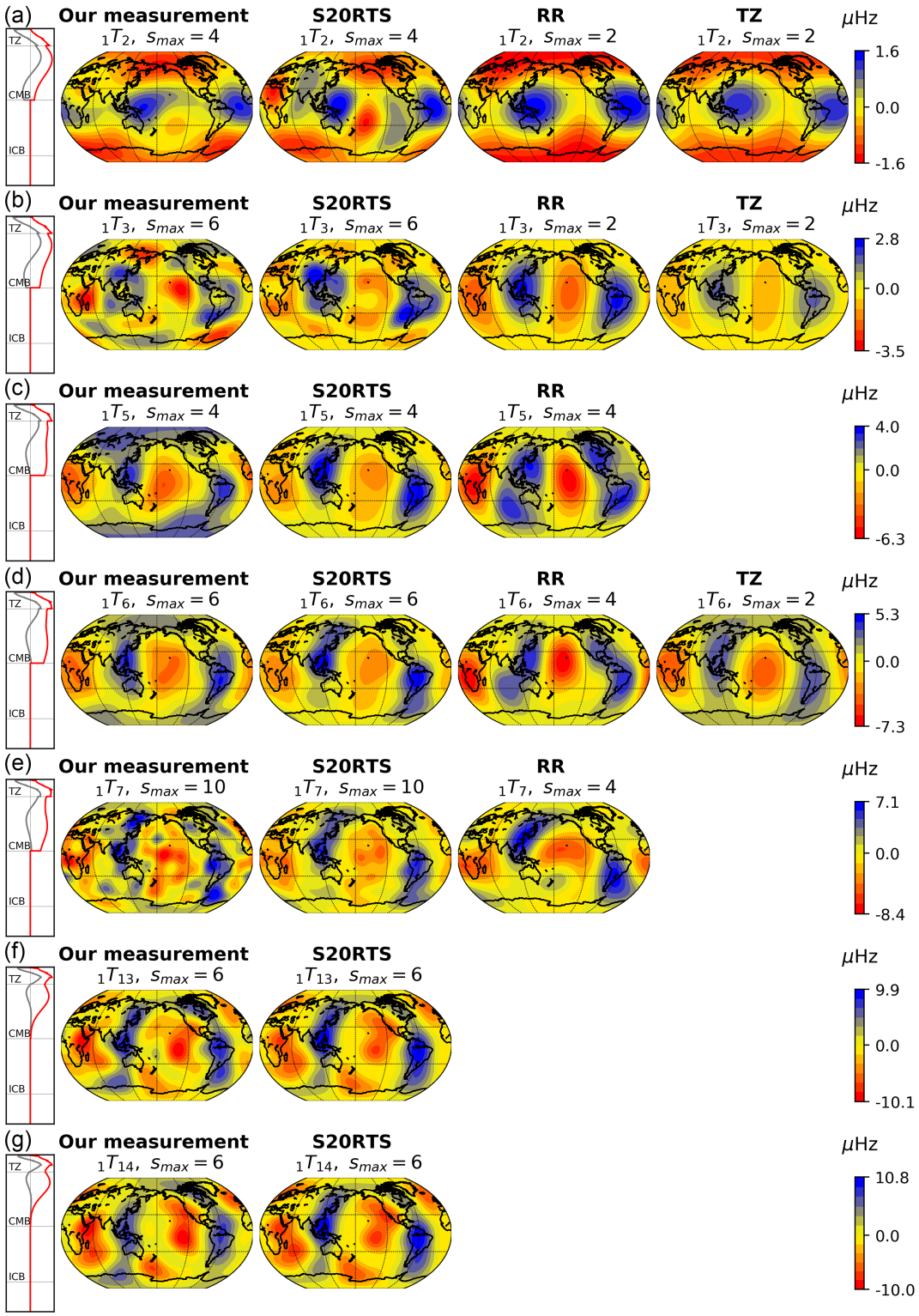

Figure 8. Our measured splitting functions compared to measurements of Resovsky & Ritzwoller (1998) and Tromp & Zanzerkia (1995) and the predictions of mantle model S20RTS and CRUST5.1. Also shown are the degree $s = 0$ sensitivity kernels K_s (v_s in red and ρ in grey) and the maximum spherical degree $s_{\max}$ for each mode.

predictions. Also for the third and fourth overtone the S20RTS model overpredicts the values for $\mathrm{Re}c_{21}$. Mantle model S20RTS is an isotropic shear wave velocity model made using Rayleigh waves and spheroidal mode splitting functions; the differences between our toroidal-mode measurements and the model predictions could be due to anisotropy.

The regional variations in frequency of the splitting functions are most easily seen in splitting function maps (Figs 8–10). Most of

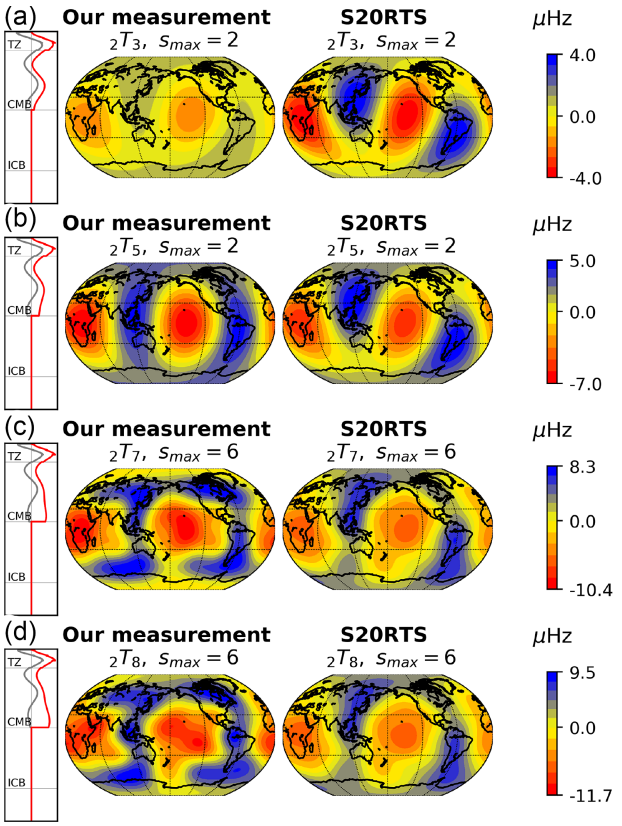

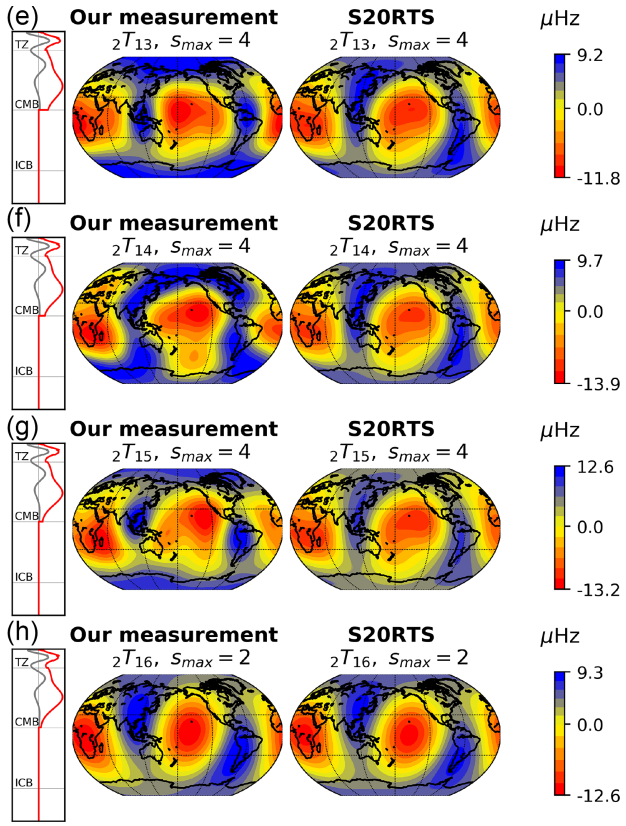

Figure 9. Same as Fig. 8, but also for the second overtone.

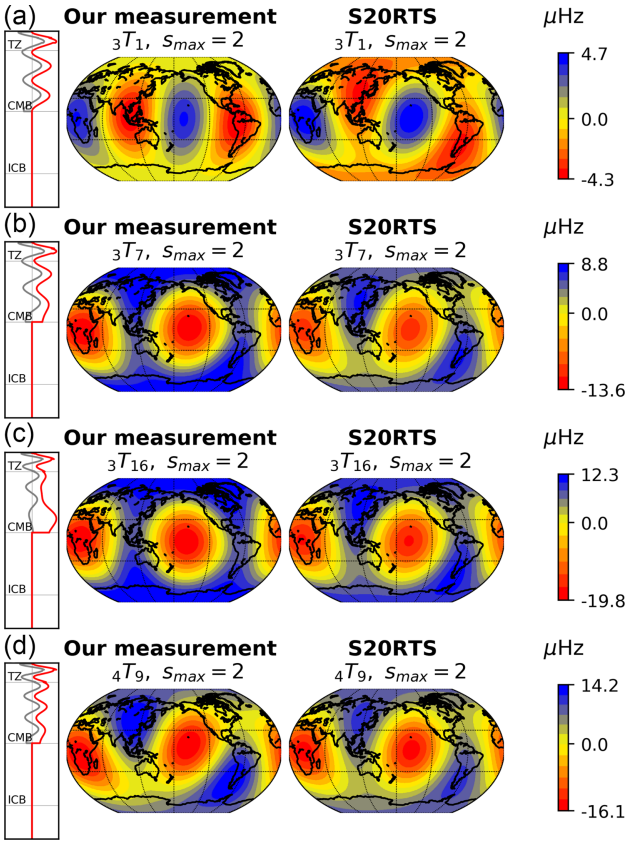

Figure 10. Same as Fig. 8, but also for the third and fourth overtones.

our measured toroidal overtones are sensitive to the whole mantle. Only for the first and second overtones the largest angular order modes have diminishing sensitivity to the core–mantle boundary. Our splitting function maps for the first overtone branch (Fig. 8) show a similar pattern as predicted by S20RTS, with the signature 'ring around the Pacific' of high-frequency anomalies surrounding a low-frequency anomaly in the centre of the Pacific. However, the splitting function maps differ in details. For example, mode $_1T_3$ (Fig. 8b) shows much stronger low-frequency anomalies in the Pacific and southern Indian ocean than the S20RTS prediction.

Due to the size of our new data set we are able to measure all modes to the same or higher degree as previously done. For example, we measured $_1T_7$ (Fig. 8e) up to degree 10, revealing more details around the Pacific and underneath Africa than previous measurements by Resovsky & Ritzwoller (1998) which were only up to degree 4. But also in comparison with the S20RTS prediction (also up to degree 10), we still see more detailed anomalies. The sensitivity kernels for this mode have a peak in the transition zone, which may suggest that more detailed slab signatures are visible in our splitting function for $_1T_7$.

Splitting function maps for toroidal modes of the second overtone branch, which have two peaks in their sensitivity kernels in the upper and lower mantle, are shown in Fig. 9. These modes (except for $_2T_8$ which was measured by Resovsky & Ritzwoller 1998) have not been measured before, so we can only compare our measurements to S20RTS predictions. Again, we observe overall the 'ring around the Pacific', which can be seen in all our measurements and S20RTS predictions, indicating the robustness of our results. However, our measured splitting functions provide a better fit to the data (see Table 2) than S20RTS and indeed the details of the ring around the Pacific structure differ. For example modes $_2T_7$ and $_2T_8$, which

have very similar sensitive kernels, both show striking differences compared to S20RTS, especially in the higher frequency anomalies near the North and South pole. Also modes ${}_2T_{13} - {}_2T_{15}$ show interestingly similar stronger anomalies near the poles, but with different overall shape than ${}_2T_7$ and ${}_2T_8$. This can also be seen in the larger observed c_{20} values in comparison to S20RTS predictions of these second overtone branch toroidal modes (Fig. 7).

Fig. 10 shows our observed splitting function maps of the third and fourth overtones, again compared to S20RTS. These modes are difficult to observe in the frequency spectrum and therefore we were only able to make robust measurements up to degree 2. These overtones are sensitive to the whole mantle and even though they are difficult to measure, they show similar features as compared to S20RTS. We do observe stronger amplitudes of the anomalies than in the S20RTS predictions. This is visible both in the splitting function maps (Fig. 10) as well as in the values of our measured degree coefficients c_{20} and Rec_{22} and Imc_{22} (Fig. 7).

5 DISCUSSION AND CONCLUSIONS

We made a new catalogue of splitting function coefficients for 19 toroidal modes from the first, second, third and fourth overtone branches, of which 13 had not been measured before. Our splitting function measurements are available online at http://www.geo.uu.nl/~deuss/research/splitting-functions. Our data set contains toroidal-mode overtones with sensitivity to upper- and lower-mantle shear wave velocity and density. The difference between our measurements, previous studies and the predictions for models S20RTS and S40RTS demonstrate the importance and potential of our toroidal-overtone measurements in improving constraints on isotropic and anisotropic mantle shear wave velocity.

ACKNOWLEDGEMENTS

We thank Gabi Laske, Caroline Beghein and Rudolf Widmer-Schnidrig for their constructive comments which helped to improve the manuscript This project has received funding from the European Research Council (ERC) under the European Union's Horizon 2020 research and innovation programme (grant agreement no. 681535—ATUNE) and a Vici award number 016.160.310/526 from the Netherlands organisation for scientific research (NWO). The facilities of IRIS Data Services, and specifically the IRIS Data Management Center, were used for access to waveforms and related metadata used in this study. IRIS Data Services are funded through the Seismological Facilities for the Advancement of Geoscience and EarthScope (SAGE) Proposal of the National Science Foundation under Cooperative Agreement EAR-1261681. We also acknowledge the use of the 'Global CMT project' webpage for the earthquake source parameters used in this study (Dziewonski *et al.* 1981; Ekström *et al.* 2012). The data analysis and figures were generated using Python (Van Rossum & Drake 2009), the Python library ObsPy (Beyreuther *et al.* 2010) and a Python package designed by SS, Lisanne Jagt and Sujania Talavera-Soza.

REFERENCES

Beghein, C., Resovsky, J. & Van Der Hilst, R.D., 2008. The signal of mantle anisotropy in the coupling of normal modes, *J. geophys. Int.,* **175**(3), 1209–1234.

Beyreuther, M., Barsch, R., Krischer, L., Megies, T., Behr, Y. & Wassermann, J., 2010. Obspy: a Python toolbox for seismology, *Seismol. Res. Lett.,* **81**(3), 530–533.

Chang, S.-J., Ferreira, A.M., Ritsema, J., van Heijst, H.J. & Woodhouse, J.H., 2014. Global radially anisotropic mantle structure from multiple datasets: a review, current challenges, and outlook, *Tectonophysics,* **617,** 1–19.

Derr, J.S., 1969. Free oscillation observations through 1968, *Bull. seism. Soc. Am.,* **59**(5), 2079–2099.

Deuss, A., Irving, J.C. & Woodhouse, J.H., 2010. Regional variation of inner core anisotropy from seismic normal mode observations, *Science,* **328**(5981), 1018–1020.

Deuss, A., Ritsema, J. & van Heijst, H., 2013. A new catalogue of normal-mode splitting function measurements up to 10 mhz, *J. geophys. Int.,* **193**(2), 920–937.

Deuss, A. & Woodhouse, J.H., 2001. Theoretical free-oscillation spectra: the importance of wide band coupling, *J. geophys. Int.,* **146**(3), 833–842.

Durek, J.J. & Romanowicz, B., 1999. Inner core anisotropy inferred by direct inversion of normal mode spectra, *J. geophys. Int.,* **139**(3), 599–622.

Dziewonski, A., Chou, T.-A. & Woodhouse, J.H., 1981. Determination of earthquake source parameters from waveform data for studies of global and regional seismicity, *J. geophys. Res.: Solid Earth,* **86**(B4), 2825–2852.

Dziewonski, A.M. & Anderson, D.L., 1981. Preliminary reference Earth model, *Phys. Earth planet. Inter.,* **25**(4), 297–356.

R.Edmonds, A., 1960. Angular momentum in quantum theory, *Princeton University Press,* Princeton, NJ.

Ekström, G. & Dziewonski, A.M., 1998. The unique anisotropy of the Pacific upper mantle, *Nature,* **394**(6689), 168–172.

Ekström, G., Nettles, M. & Dziewoński, A., 2012. The global CMT project 2004–2010: centroid-moment tensors for 13,017 earthquakes, *Phys. Earth planet. Inter.,* **200,** 1–9.

French, S. & Romanowicz, B., 2014. Whole-mantle radially anisotropic shear velocity structure from spectral-element waveform tomography, *J. geophys. Int.,* **199**(3), 1303–1327.

Giardini, D., Li, X.-D. & Woodhouse, J.H., 1988. Splitting functions of long-period normal modes of the Earth, *J. geophys. Res.: Solid Earth,* **93**(B11), 13716–13742.

He, X. & Tromp, J., 1996. Normal-mode constraints on the structure of the Earth, *J. geophys. Res.: Solid Earth,* **101**(B9), 20053–20082.

Igel, H., Nader, M.-F., Kurrle, D., Ferreira, A.M., Wassermann, J. & Schreiber, K.U., 2011. Observations of Earth's toroidal free oscillations with a rotation sensor: the 2011 magnitude 9.0 Tohoku-Oki Earthquake, *Geophys. Res. Lett.,* **38**(21), doi:10.1029/2011GL049045.

Ishii, M. & Tromp, J., 1999. Normal-mode and free-air gravity constraints on lateral variations in velocity and density of Earth's mantle, *Science,* **285**(5431), 1231–1236.

Koelemeijer, P., Deuss, A. & Ritsema, J., 2013. Observations of core-mantle boundary Stoneley modes, *Geophys. Res. Lett.,* **40**(11), 2557–2561.

Koelemeijer, P., Deuss, A. & Ritsema, J., 2017. Density structure of Earth's lowermost mantle from Stoneley mode splitting observations, *Nat. Commun.,* **8**(1), 1–10.

Koelemeijer, P., Ritsema, J., Deuss, A. & Van Heijst, H.-J., 2015. Sp12rts: a degree-12 model of shear-and compressional-wave velocity for Earth's mantle, *J. geophys. Int.,* **204**(2), 1024–1039.

Kuo, C. & Romanowicz, B., 2002. On the resolution of density anomalies in the Earth's mantle using spectral fitting of normal-mode data, *J. geophys. Int.,* **150**(1), 162–179.

Lebedev, S., Boonen, J. & Trampert, J., 2009. Seismic structure of Precambrian lithosphere: new constraints from broad-band surface-wave dispersion, *Lithos,* **109**(1–2), 96–111.

Long, M.D. & Becker, T.W., 2010. Mantle dynamics and seismic anisotropy, *Earth planet. Sci. Lett.,* **297**(3–4), 341–354.

Marone, F. & Romanowicz, B., 2007. The depth distribution of azimuthal anisotropy in the continental upper mantle, *Nature,* **447**(7141), 198–201.

Masters, G., Laske, G. & Gilbert, F., 2000a. Autoregressive estimation of the splitting matrix of free-oscillation multiplets, *J. geophys. Int.,* **141**(1), 25–42.

Masters, G., Laske, G. & Gilbert, F., 2000b. Matrix autoregressive analysis of free-oscillation coupling and splitting, *J. geophys. Int.,* **143**(2), 478–489.

Masters, T. & Widmer, R., 1995. Free oscillations: frequencies and attenuations, *Global Earth Physics: A Handbook of Physical Constants,* Vol. **1,** p. 104, American Geophysical Union, DOI:10.1029/RF001.

Montagner, J.-P. & Tanimoto, T., 1991. Global upper mantle tomography of seismic velocities and anisotropies, *J. geophys. Res.: Solid Earth,* **96**(B12), 20337–20351.

Moulik, P. & Ekström, G., 2014. An anisotropic shear velocity model of the Earth's mantle using normal modes, body waves, surface waves and long-period waveforms, *J. geophys. Int.,* **199**(3), 1713–1738.

Mäkinen, A.M. & Deuss, A., 2013. Normal mode splitting function measurements of anelasticity and attenuation in the Earth's inner core, *J. geophys. Int.,* **194**(1), 401–416.

Pachhai, S., Tkalčić, H. & Masters, G., 2015. Estimation of splitting functions from Earth's normal mode spectra using the neighbourhood algorithm, *J. geophys. Int.,* **204**(1), 111–126.

Panning, M. & Romanowicz, B., 2006. A three-dimensional radially anisotropic model of shear velocity in the whole mantle, *J. geophys. Int.,* **167**(1), 361–379.

Resovsky, J. & Trampert, J., 2003. Using probabilistic seismic tomography to test mantle velocity–density relationships, *Earth planet. Sci. Lett.,* **215**(1–2), 121–134.

Resovsky, J.S. & Ritzwoller, M.H., 1998. New and refined constraints on three-dimensional Earth structure from normal modes below 3 mhz, *J. geophys. Res.: Solid Earth,* **103**(B1), 783–810.

Ringler, A.T., Steim, J., van Zandt, T., Hutt, C.R., Wilson, D.C. & Storm, T., 2015. Potential improvements in horizontal very broadband seismic data in the IRIS/USGS component of the global seismic network, *Seismol. Res. Lett.,* **87**(1), 81–89.

Ringler, A.T., Wilson, D.C., Storm, T., Marshall, B., Hutt, C.R. & Holland, A., 2016. Noise reduction in long-period seismograms by way of array summing, *Bull. seism. Soc. Am.,* **106**(5), 1991–1997.

Ritsema, J., Deuss, A.A., Van Heijst, H. & Woodhouse, J., 2011. S40rts: a degree-40 shear-velocity model for the mantle from new Rayleigh wave dispersion, teleseismic traveltime and normal-mode splitting function measurements, *J. geophys. Int.,* **184**(3), 1223–1236.

Roult, G., ,Romanowicz, B. & Montagner, J.P. 1990. 3-D upper mantle shear velocity and attenuation from fundamental mode free oscillation data, *Geophysical Journal International,* **101,** 1, 61–80.

Russell, J.B., Gaherty, J.B., Lin, P.-Y.P., Lizarralde, D., Collins, J.A., Hirth, G. & Evans, R.L., 2019. High-resolution constraints on pacific upper mantle petrofabric inferred from surface-wave anisotropy, *J. geophys. Res.: Solid Earth,* **124**(1), 631–657.

Schaeffer, A., Lebedev, S. & Becker, T., 2016. Azimuthal seismic anisotropy in the Earth's upper mantle and the thickness of tectonic plates, *Geophys. Suppl. Mon. Not. R. Astron. Soc.,* **207**(2), 901–933.

Smith, M.L. & Dahlen, F., 1973. The azimuthal dependence of Love and Rayleigh wave propagation in a slightly anisotropic medium, *J. geophys. Res.,* **78**(17), 3321–3333.

Steffen, H., Kuhlmann, S., Jahr, T. & Kroner, C., 2006. Numerical modelling of the barometric pressure-induced noise in horizontal components for the observatories Moxa and Schiltach, *J. Geodyn.,* **41**(1–3), 242–252.

Tanimoto, T. & Anderson, D.L., 1985. Lateral heterogeneity and azimuthal anisotropy of the upper mantle: Love and Rayleigh waves 100–250 s, *J. geophys. Res.: Solid Earth,* **90**(B2), 1842–1858.

Tarantola, A. & Valette, B., 1982. Generalized nonlinear inverse problems solved using the least squares criterion, *Rev. Geophys.,* **20**(2), 219–232.

Trampert, J., Deschamps, F., Resovsky, J. & Yuen, D., 2004. Probabilistic tomography maps chemical heterogeneities throughout the lower mantle, *Science,* **306**(5697), 853–856.

Trampert, J. & van Heijst, H.J., 2002. Global azimuthal anisotropy in the transition zone, *Science,* **296**(5571), 1297–1299.

Tromp, J. & Zanzerkia, E., 1995. Toroidal splitting observations from the great 1994 Bolivia and Kuril Islands Earthquakes, *Geophys. Res. Lett.,* **22**(16), 2297–2300.

Van Rossum, G. & Drake, F.L., 2009. *Python 3 Reference Manual,* CreateSpace, Scotts Valley, CA.

Vinnik, L., Breger, L. & Romanowicz, B., 1998. Anisotropic structures at the base of the Earth's mantle, *Nature,* **393**(6685), 564–567.

Widmer, R., Zürn, W. & Masters, G., 1992. Observation of low-order toroidal modes from the 1989 Macquarie Rise event, *J. geophys. Int.,* **111**(2), 226–236.

Woodhouse, J., 1980. The coupling and attenuation of nearly resonant multiplets in the Earth's free oscillation spectrum, *J. geophys. Int.,* **61**(2), 261–283.

Woodhouse, J. & Giardini, D., 1985. Inversion for the splitting functions of isolated normal mode multiplets, *EOS, Trans. Am. geophys. Un.,* **66,** 301–301.

Yuan, K. & Beghein, C., 2014. Three-dimensional variations in Love and Rayleigh wave azimuthal anisotropy for the upper 800 km of the mantle, *J. geophys. Res.: Solid Earth,* **119**(4), 3232–3255.

Zürn, W., Ferreira, A., Widmer-Schnidrig, R., Lentas, K., Rivera, L. & Clévédé, E., 2015. High-quality lowest-frequency normal mode strain observations at the Black Forest Observatory (SW-Germany) and comparison with horizontal broad-band seismometer data and synthetics, *Geophys. Suppl. Mon. Not. R. Astron. Soc.,* **203**(3), 1787–1803.